Supporting Information

Coupling pentlandite nanoparticles and dual-doped carbon networks to yield efficient and stable electrocatalysts for acid water oxidation

Qi Hu, Guodong Li, Xiufang Liu, Bin Zhu, Guomin Li, Liangdong Fan, Xiaoyan Chai, Qianling Zhang, Jianhong Liu and Chuanxin He*

College of Chemistry and Environmental Engineering, Shenzhen University, Shenzhen, Guangdong, 518060, People's Republic of China.

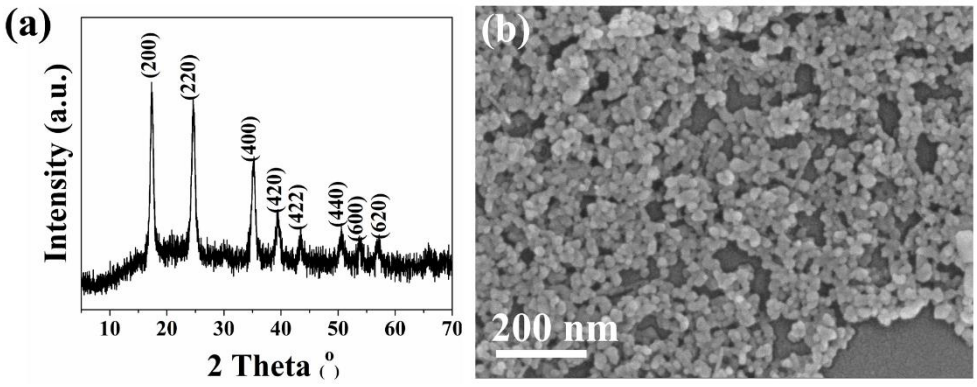

Figure S1 (a) XRD pattern of binary NiFe-Prussian blue analogues (denoted NiFe-PBAs), (b) SEM image of NiFe-PBAs

The XRD pattern of NiFe-PBAs showed a set of diffraction peaks, corresponding to (200), (220), (400), (420), (422), (440), (660) and (620) planes for PBAs (JCPDS no. 20-0915) (Figure S1a), indicating the successful synthesis of PBAs.

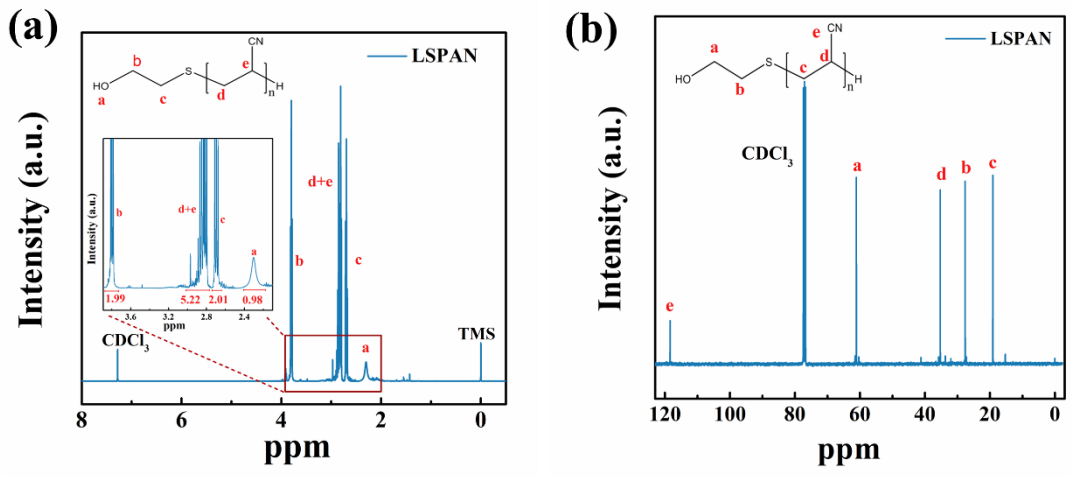

Figure S2 (a) ^{1}H and (b) ^{13}C NMR spectra of liquid sulfur-modified-polyacrylonitrile (denoted LSPAN).

The molecular structure of as-synthesized LSPAN was investigated by NMR spectra. The ^{1}H spectrum of LSPAN displayed a set of peaks, in well accordance with structure of LSPAN (Figure S2a). Based on the ration of different peaks, the degree of polymerization (DP) for LSPAN was calculated to be 1 and 2. In the case of ^{13}C NMR spectrum for LSPAN, obvious peaks for C≡N carbons (~120 ppm) and C-H carbons (i.e. a, b, c and d peaks ranging from 20 to 60 ppm) can be found in Figure S2b, further confirming the successful synthesis of LSPAN with low DP (i.e. 1 and 2).

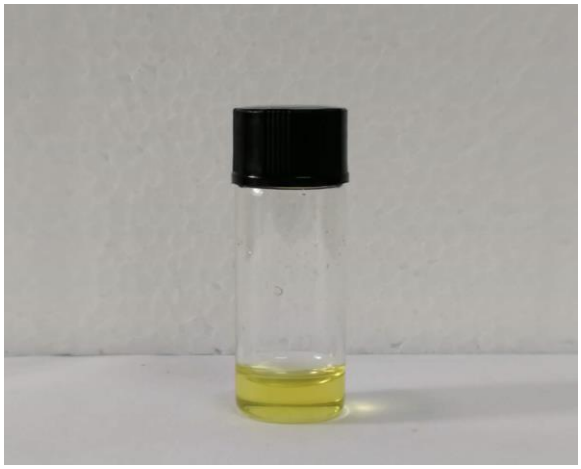

Figure S3 Optical image of as-synthesized LSPAN with low DP (i.e. 1 and 2)

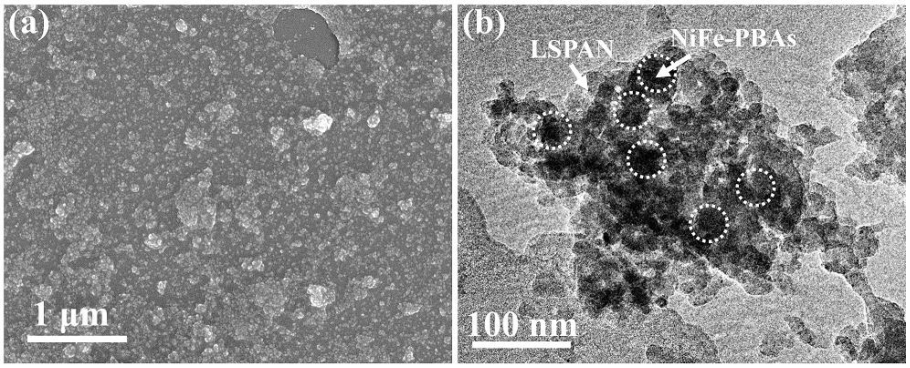

Figure S4 (a) SEM and (b) TEM images of NiFe-PBAs/LSPAN hybrid precursors.

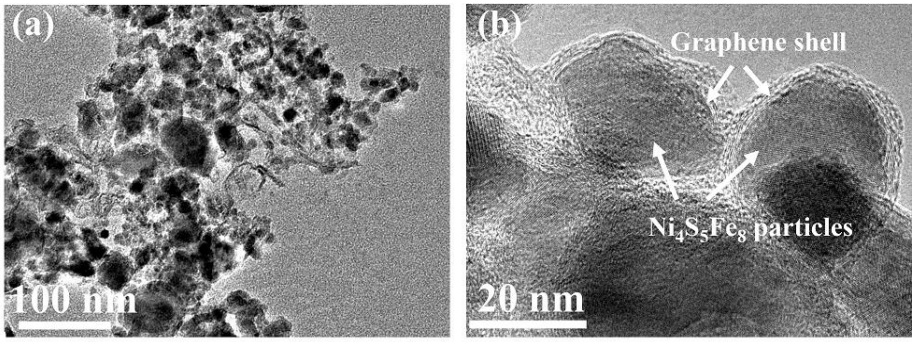

Figure S5 (a) SEM and (b) TEM images of N, S-doped carbon network-immobilized large pentlandites (i.e. $Ni_4Fe_5S_8$) nanoparticles (denoted NSC/$Ni_4Fe_5S_8$-1000). The NSC/$Ni_4Fe_5S_8$-1000 was synthesized through pyrolysis of NiFe-PBAs/LSPAN hybrid precursors at 1000 ºC under argon atmosphere.

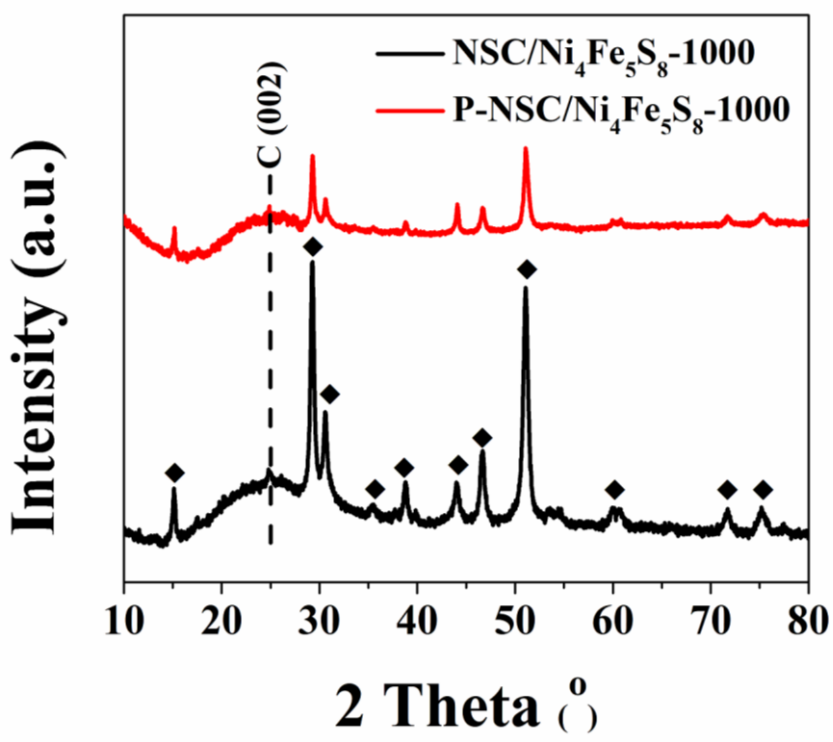

Figure S6 XRD patterns of NSC/$Ni_4Fe_4S_8$-1000 and P-NSC/$Ni_4Fe_4S_8$-1000. The P-NSC/$Ni_4Fe_4S_8$-1000 was synthesized by acid etching of NSC/$Ni_4Fe_4S_8$-1000.

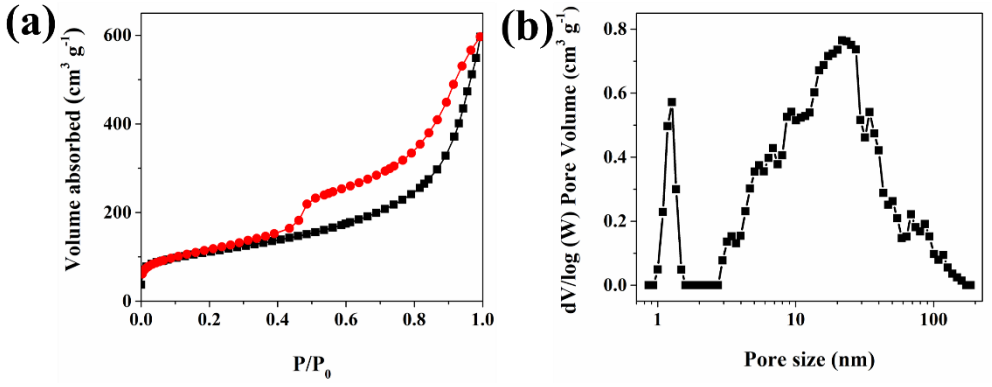

Figure S7 (a) N_2 adsorption-desorption isotherms of P-NSC/$Ni_4Fe_5S_8$-1000 (with porous structure) at 77 K, (b) corresponding pore distribution of P-NSC/$Ni_4Fe_5S_8$-1000 determined by the method of density functional theory.

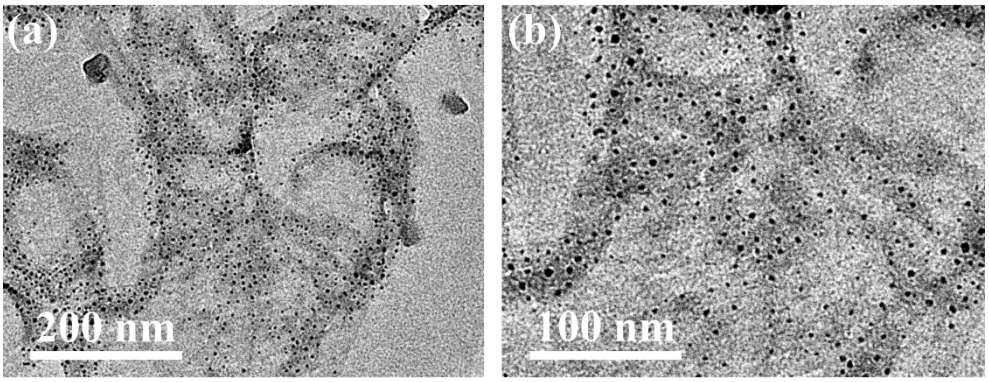

Figure S8 TEM images of P-NSC/$Ni_4Fe_5S_8$-1000 sample after further acid etching in 1 M H_2SO_4 solution at 100 ºC for 24 h.

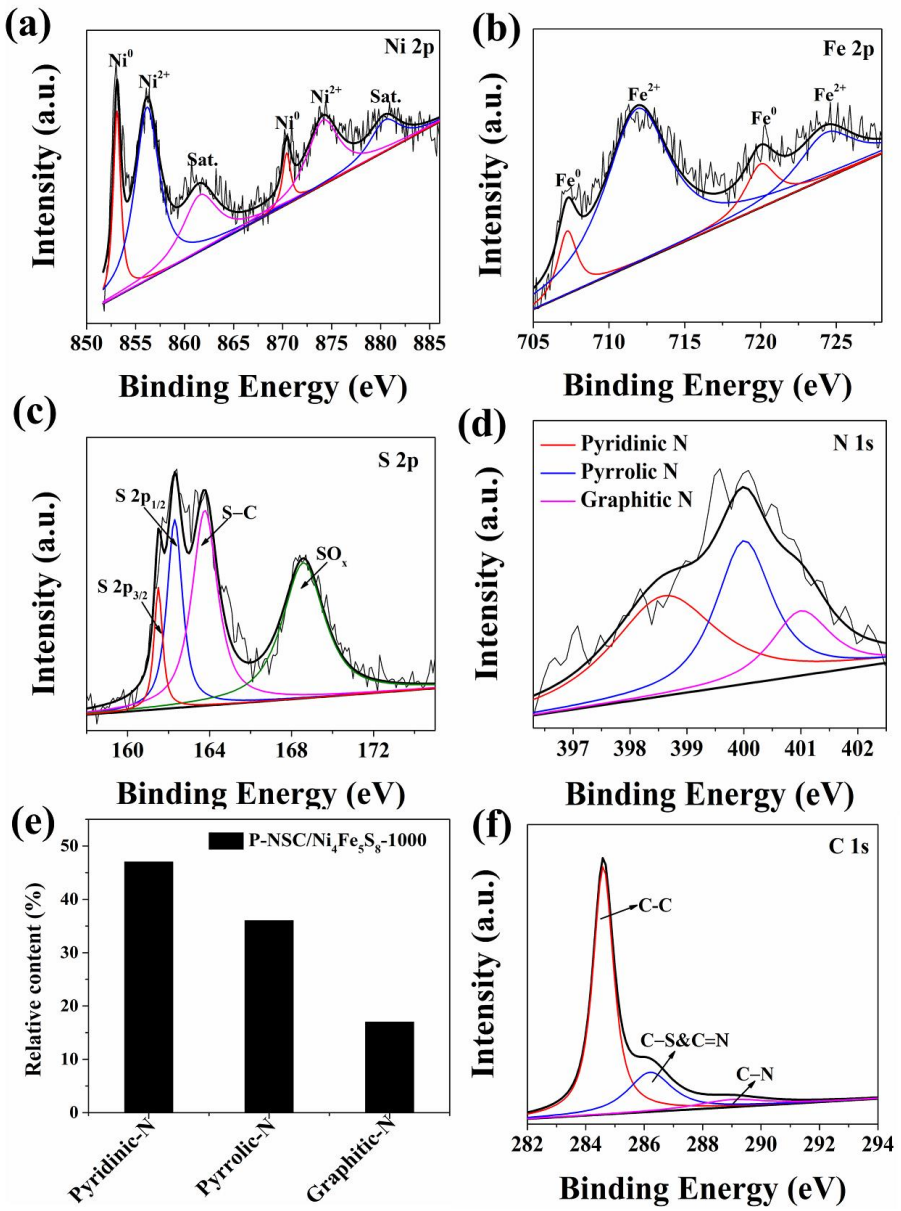

Figure S9 XPS spectrum of (a) Ni 2p, (b) Fe 2p, (c) S 2p, (d) N 1s, (e) distribution of different N species (i.e. pyridinic-N, pyrrolic-N, and graphitic-N) based on (d), and (f) C 1s for P-NSC/$Ni_4Fe_4S_8$-1000 (with porous structure).

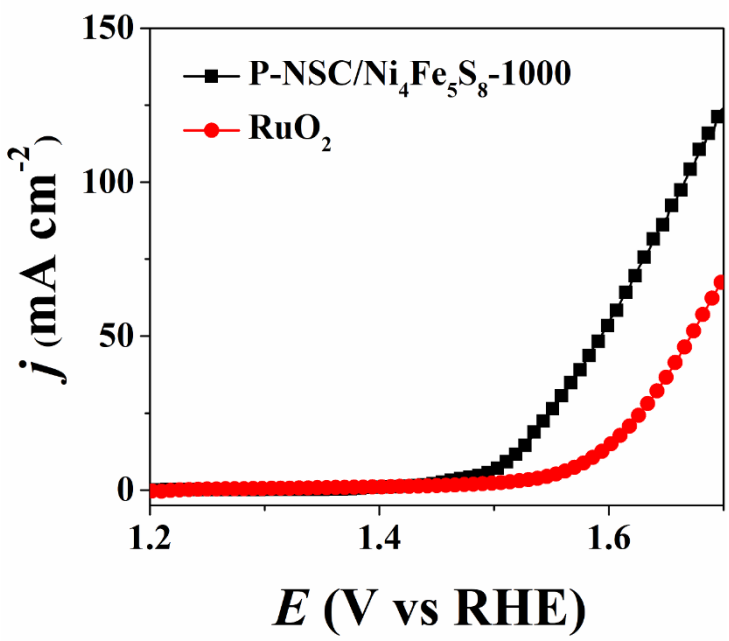

Figure S10 Steady-state polarization curves of P-NSC/$Ni_4Fe_5S_8$-1000 and commercial RuO_2 electrocatalysts for OER in 1 M KOH.

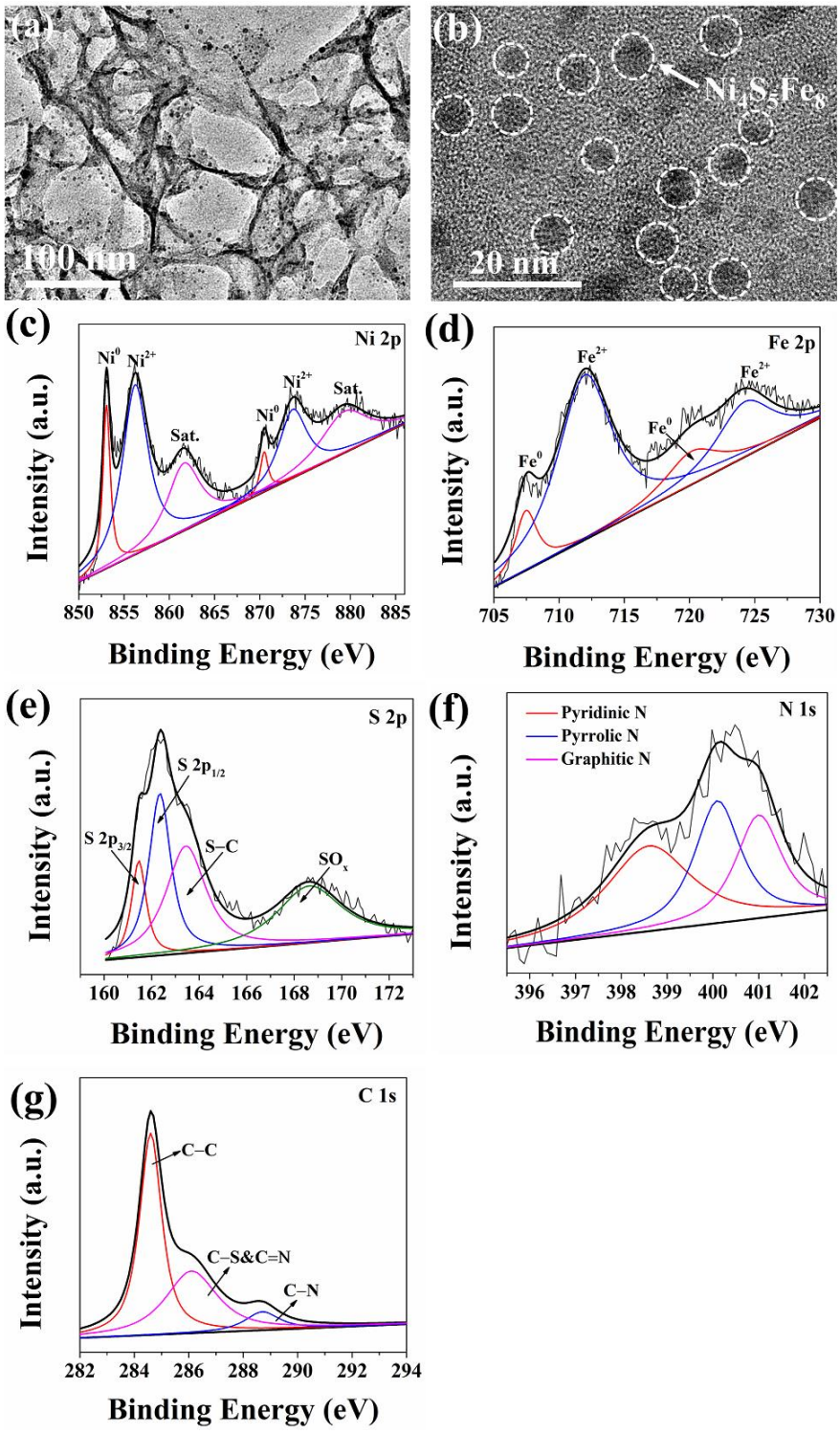

Figure S11 (a) TEM and (b) HRTEM images of P-NSC/$Ni_4Fe_4S_8$-1000 after 10000 times of potential cycles between 1.2 and 1.9 V (vs RHE). XPS spectra of (c) Ni 2p, (d) Fe 2p, (e) S 2p, (f) N 1s and (g) C 1s for P-NSC/$Ni_4Fe_4S_9$-1000 after 10000 times of potential cycles.

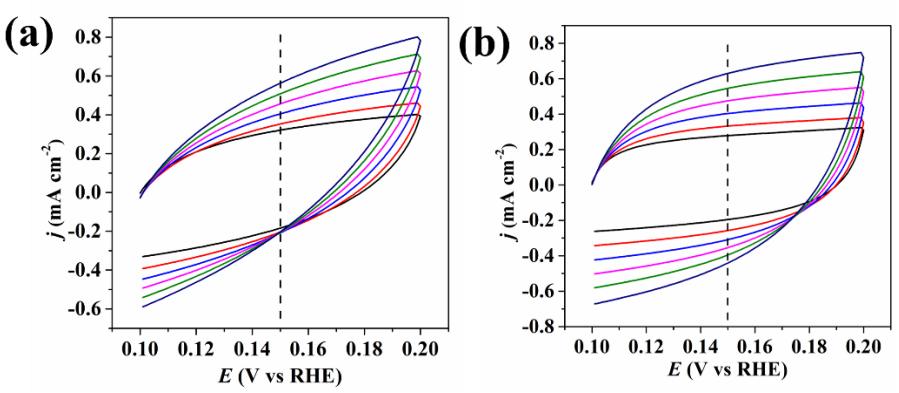

Figure S12 CV curves for (a) NSC/$Ni_4Fe_4S_8$-1000 (without porous structure) and (b) P-NSC/$Ni_4Fe_4S_8$-1000 (with porous structure) at different rates (i.e. 0.04, 0.06, 0.08, 0.10, 0.12, and 0.14 V/s).

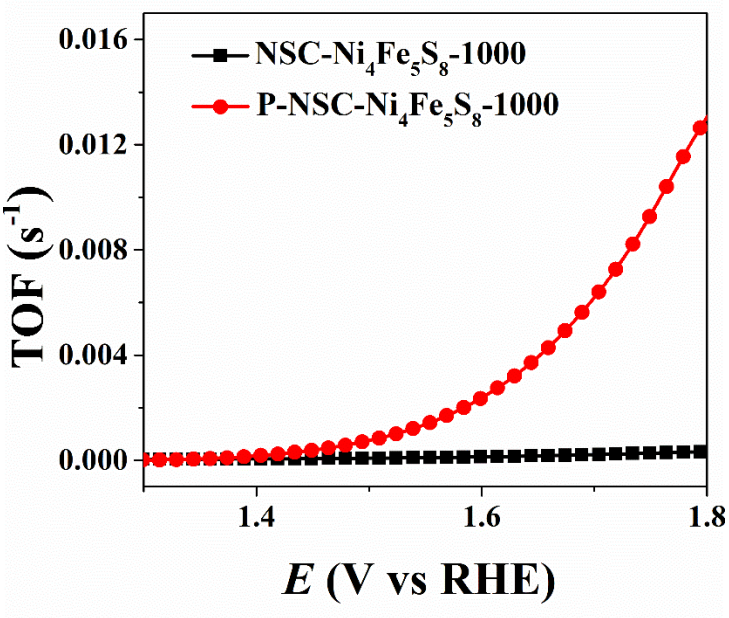

Figure S13 Plots of TOF for NSC/$Ni_4Fe_4S_8$-1000 and P-NSC/$Ni_4Fe_4S_8$-1000 against different potentials.

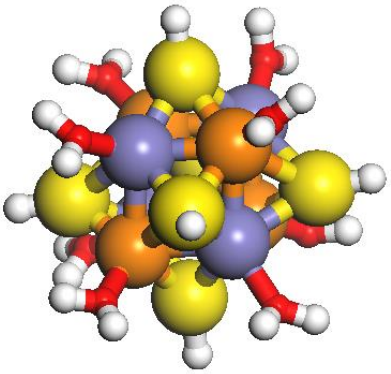

Figure S14 Structure scheme of $H_6Fe_4Ni_4S_6(H_2O)_8^{2+}$ clusters determined by computational modeling. Lavender, orange, yellow, white, and red represent Fe, Ni, S, H, and O atoms, respectively.

$$H_2O + M \longrightarrow OH^*\text{-}M + H^+ + e^-$$

$$OH^*\text{-}M \longrightarrow O^*\text{-}M + H^+ + e^-$$

$$O^*\text{-}M + H_2O \longrightarrow OOH^*\text{-}M + H^+ + e^-$$

$$OOH^*\text{-}M \longrightarrow M + O_2^* + H^+ + e^-$$

$$O_2^* \longrightarrow O_2 + *$$

Figure S15 Reaction process of OER in acid media.

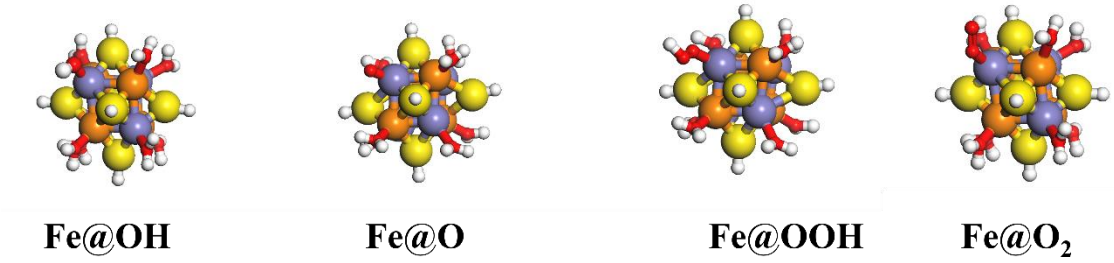

Figure S16 Atomic configurations for OER intermediates on Fe sites of $H_6Fe_4Ni_4S_6(H_2O)_8^{2+}$ clusters. Lavender, orange, yellow, white, and red represent Fe, Ni, S, H, and O atoms, respectively.

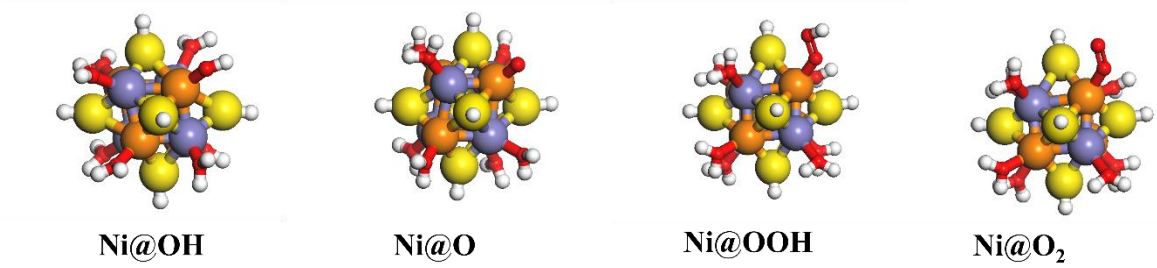

Figure S17 Atomic configurations for OER intermediates on Ni sites of $H_6Fe_4Ni_4S_6(H_2O)_8^{2+}$ clusters. Lavender, orange, yellow, white, and red represent Fe, Ni, S, H, and O atoms, respectively.

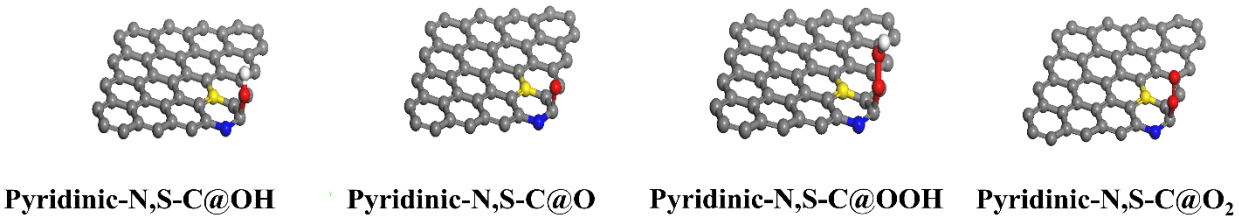

Figure S18 Atomic configurations for OER intermediates on pyridinic-N, S doped carbon (denoted pyridinic-N, S-C). Black, yellow, blue, red, and white represent to C, S, N, O, and H atoms, respectively.

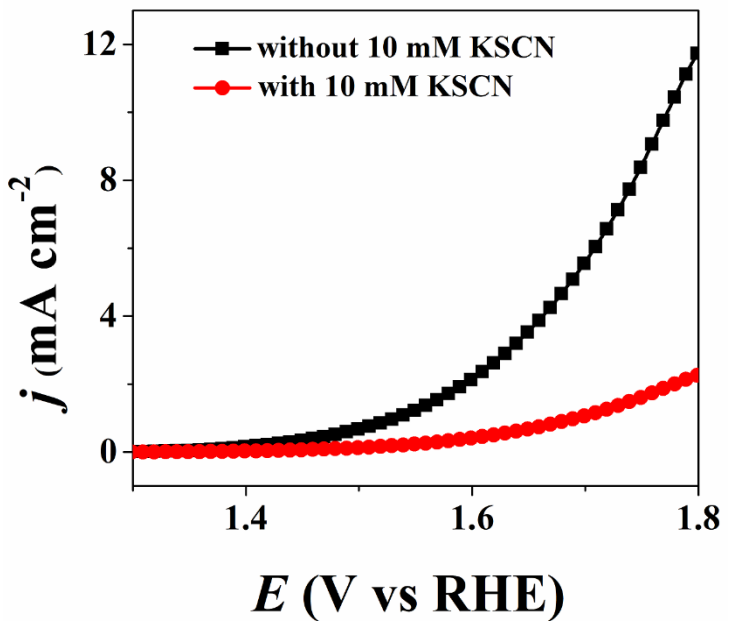

Figure S19 Steady-state polarization curves of P-NSC/$Ni_4Fe_5S_8$-1000 with and without addition of 0.01 M KSCN aqueous solution.

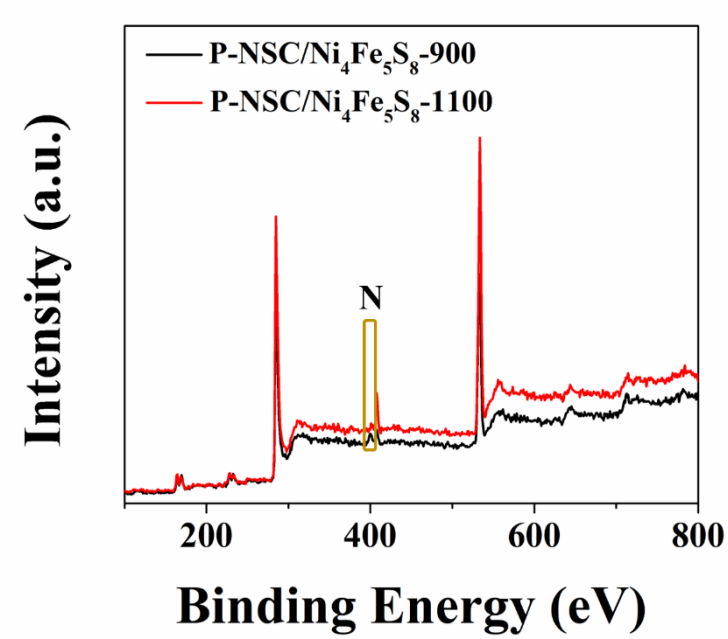

Figure S20 XPS spectra of survey for P-NSC/$Ni_4Fe_5S_8$-900 and P-NSC/$Ni_4Fe_5S_8$-1100 samples (900 and 1100 refer to the pyrolysis temperature). Both samples were synthesized through same procedure as P-NSC/$Ni_4Fe_5S_8$ except that the pyrolysis temperature changed to 900 and 1100 ºC, respectively.

Table S1 Elemental compositions of P-NSC/$Ni_4Fe_5S_8$-900 and P-NSC/$Ni_4Fe_5S_8$-1100 catalysts determined by XPS

Catalysts	**C (at%)**	**N (at%)**	**Ni (at%)**	**Fe (at%)**	**S (at%)**	**O (at%)**
P-NSC/$Ni_4Fe_5S_8$-900	64.05	2.67	2.43	1.19	5.00	24.66
P-NSC/$Ni_4Fe_5S_8$-1100	64.83	1.08	1.55	1.31	3.58	27.65

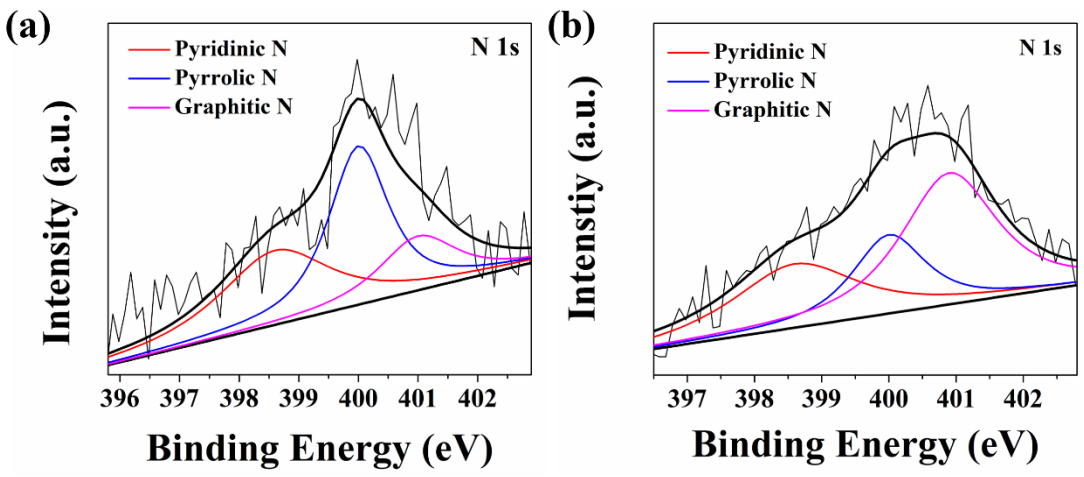

Figure S21 XPS spectra of N 1s for (a) P-NSC/$Ni_4Fe_5S_8$-900 and (b) P-NSC/$Ni_4Fe_5S_8$-1100.

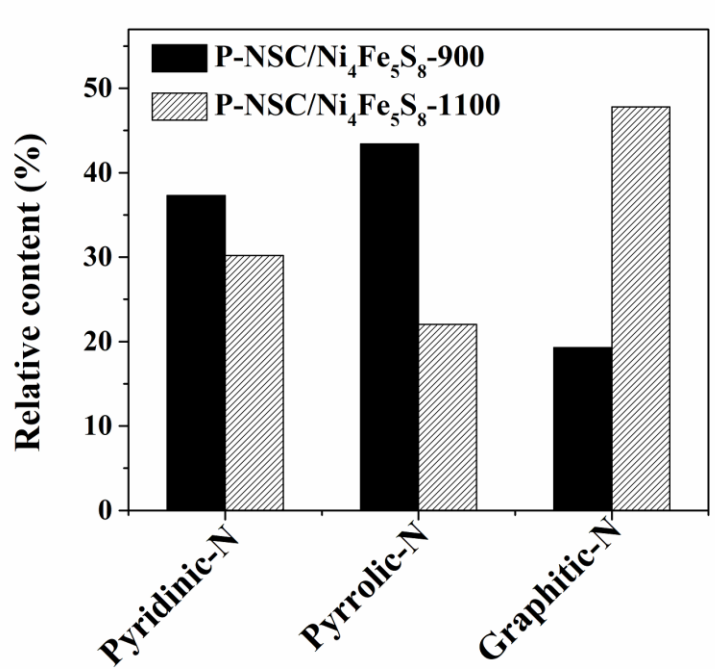

Figure S22 Distribution of pyridinic-N, pyrrolic-N, and graphitic-N determined by XPS for P-NSC/$Ni_4Fe_5S_8$-900 and P-NSC/$Ni_4Fe_5S_8$-1100.

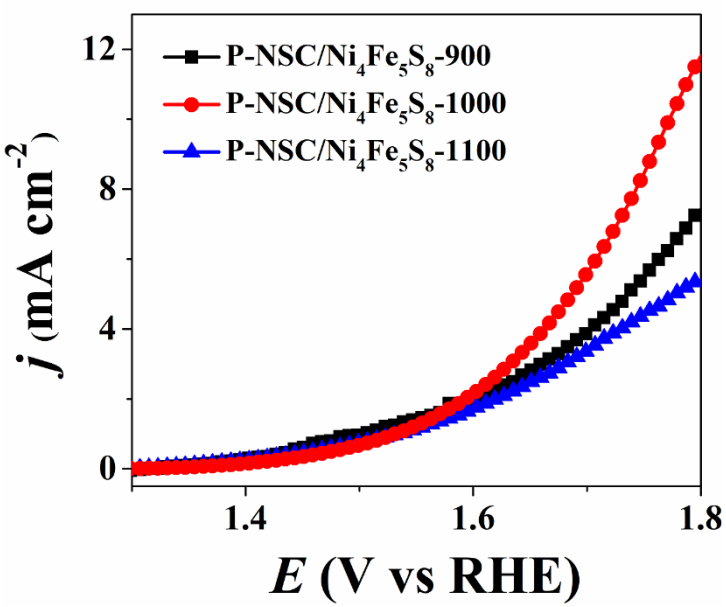

Figure S23 Steady-state polarization curves of P-NSC/$Ni_4Fe_5S_8$-900, P-NSC/$Ni_4Fe_5S_8$-1000, and P-NSC/$Ni_4Fe_5S_8$-1100 for OER in 0.5 M H_2SO_4.

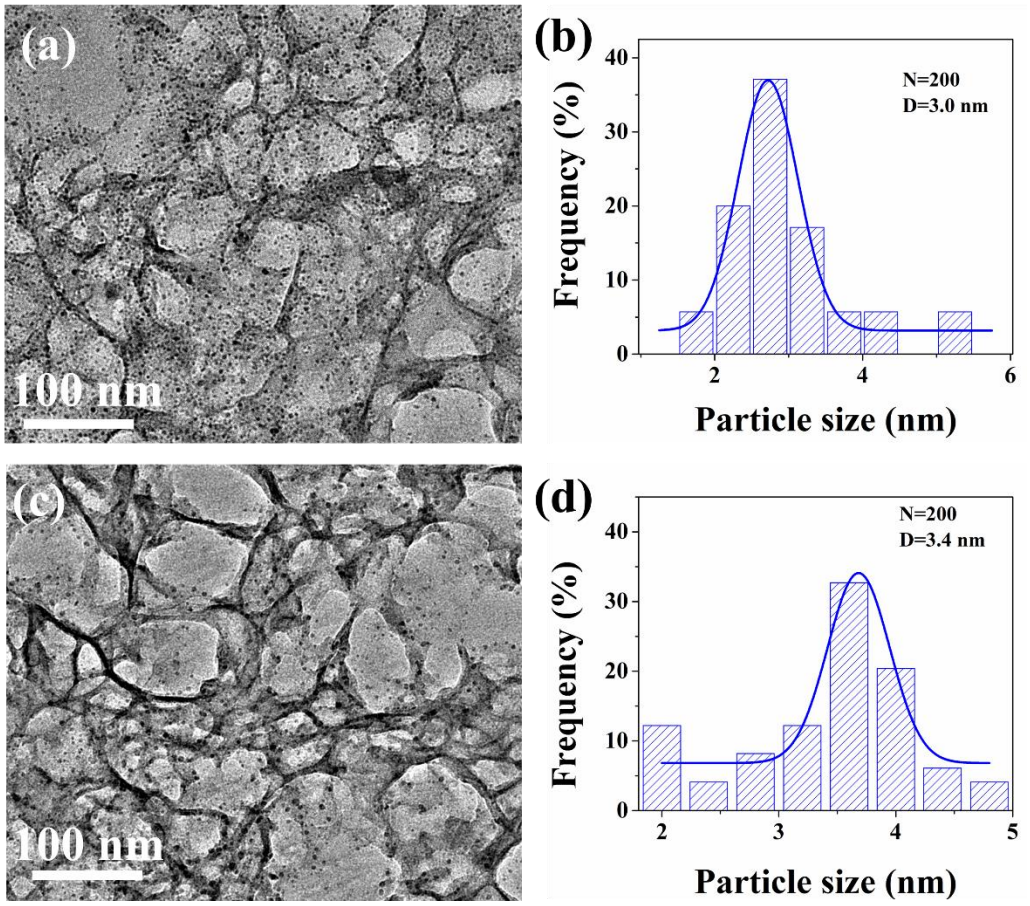

Figure S24 (a) TEM images of P-NSC/$Ni_4Fe_5S_8$-900, (b) corresponding size distribution of $Ni_4Fe_5S_8$ nanoparticles based on (a); (c) TEM images of P-NSC/$Ni_4Fe_5S_8$-1100, (d) corresponding size distribution of $Ni_4Fe_5S_8$ nanoparticles based on (c).

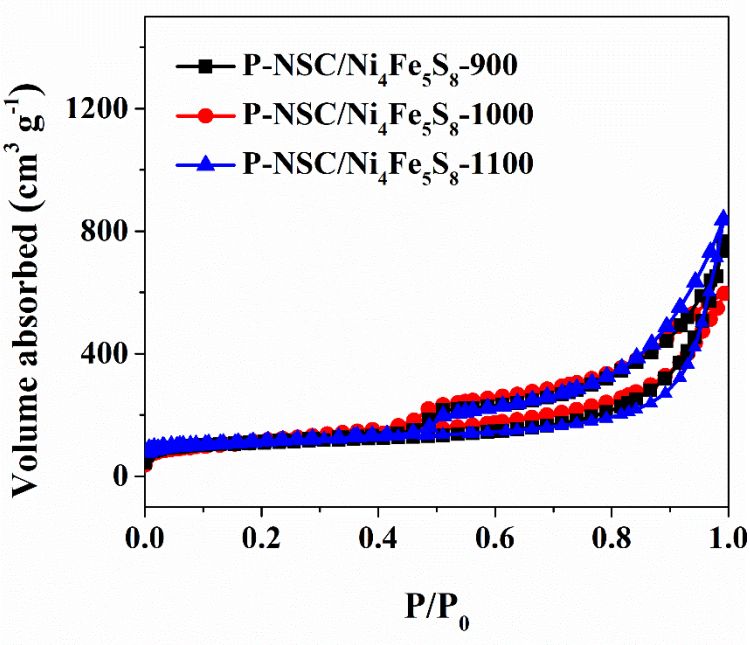

Figure S25 N_2 adsorption-desorption isotherms of P-NSC/$Ni_4Fe_5S_8$-900, P-NSC/$Ni_4Fe_5S_8$-1000, and P-NSC/$Ni_4Fe_5S_8$-1100 at 77 K.

To further examine the important role of pyridinic-N, S doped carbon for acid OER, we also prepared P-NSC/$Ni_4Fe_5S_8$-900 and P-NSC/$Ni_4Fe_5S_8$-1100 (900 and 1100 refer to the pyrolysis temperature) (see Experiment Section). With the pyrolysis temperature increase from 900 to 1100 ºC, the N contents decreased sharply from 2.67 to 1.08 at%, accompanying with the ratio of pyridinic-N to sum N decreasing from 0.37 to 0.30. (Figure S20-21, and Table S1). This means that there are much more pyridinic-N species on the P-NSC/$Ni_4Fe_5S_8$-900, compared with that of P-NSC/$Ni_4Fe_5S_8$-900. Furthermore, the content of S elements in the P-NSC/$Ni_4Fe_5S_8$-900 is 5.00 at%, higher than that on the P-NSC/$Ni_4Fe_5S_8$-1100 (3.58 at%). Given the high content of pyridinic N and S species in the P-NSC/$Ni_4Fe_5S_8$-900, it can be concluded that there are more

pyridinic-N, S-doped carbon in the P-NSC/$Ni_4Fe_5S_8$-900 than that in the P-NSC/$Ni_4Fe_5S_8$-1100. The OER performance of P-NSC/$Ni_4Fe_5S_8$-900 and P-NSC/$Ni_4Fe_5S_8$-1100 was then tested in 0.5 M H_2SO_4. (Figure S22) With the higher pyridinic-N, S-doped carbon contents, the P-NSC/$Ni_4Fe_5S_8$-900 displayed higher OER activity than that of P-NSC/$Ni_4Fe_5S_8$-1100, suggesting the essential role of pyridinic-N, S-doped carbon for OER. Nevertheless, the OER activity of P-NSC/$Ni_4Fe_5S_8$-900 is still lower than that of P-NSC/$Ni_4Fe_5S_8$-1000, further confirming the high activity of P-NSC/$Ni_4Fe_5S_8$-1000 for OER.

On the other hand, as displayed in Figure S24, the $Ni_4Fe_5S_8$ nanoparticles in all of the P-NSC/$Ni_4Fe_5S_8$ samples (i.e. P-NSC/$Ni_4Fe_5S_8$-900, P-NSC/$Ni_4Fe_5S_8$-1000, and P-NSC/$Ni_4Fe_5S_8$-1100) were in size of ~3.0 nm, indicating that the pyrolysis temperature had little impact on the size of resulting $Ni_4Fe_5S_8$ nanoparticles. Moreover, the P-NSC/$Ni_4Fe_5S_8$-900, and P-NSC/$Ni_4Fe_5S_8$-1100 displayed the similar isotherm curves as that of P-NSC/$Ni_4Fe_5S_8$-1100. (Figure S25) And, all the P-NSC/$Ni_4Fe_5S_8$-900, P-NSC/$Ni_4Fe_5S_8$-1000, and P-NSC/$Ni_4Fe_5S_8$-1100 possessed nearly the same BET surface area of ~400 cm^2 g^{-1}. Therefore, the different acid OER performance demonstrated on P-NSC/$Ni_4Fe_5S_8$-900, P-NSC/$Ni_4Fe_5S_8$-1000, and P-NSC/$Ni_4Fe_5S_8$-1100 may not be related to the particle size of $Ni_4Fe_5S_8$ and surface area. In other words, the different OER performance is solely resulted from the different content of pyridinic-N, S-doped carbon.

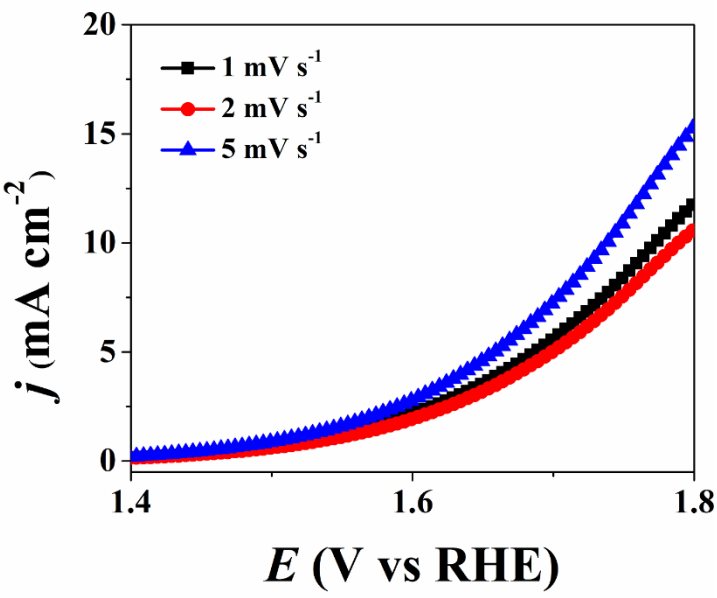

Figure S26 Steady-state polarization profiles of P-NSC/$Ni_4Fe_5S_8$-1000 for OER at different scan rates in 0.5 M H_2SO_4.

To investigate the mass transport of acid OER process, the polarization profiles of P-NSC/$Ni_4Fe_5S_8$-1000 for OER at different scan rates (i.e. 1, 2, 5 mV s^{-1}) were recorded. (Figure S26) With the scan rates increasing from 1 to 5 mV s^{-1}, only tiny change of polarization curves can be observed on P-NSC/$Ni_4Fe_5S_8$-1000 electrocatalyst, implying the fast mass transport during OER.[1]

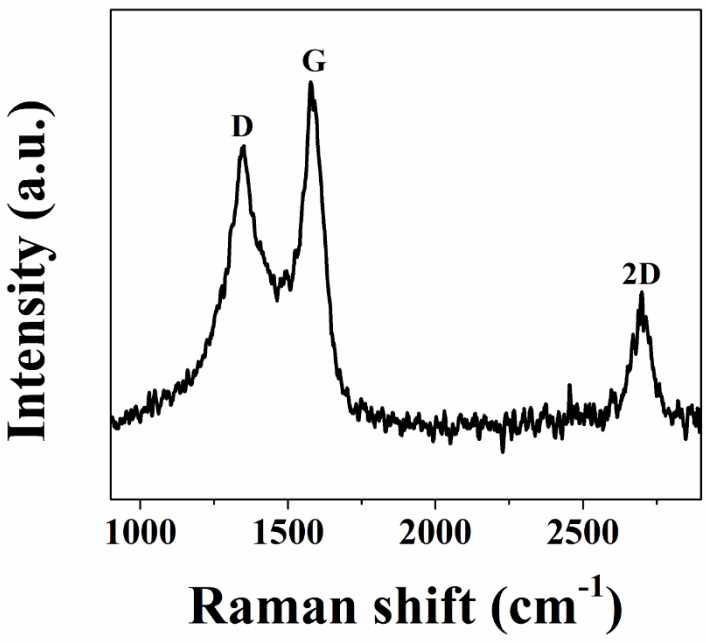

Figure S27 Raman spectrum of P-NSC/$Ni_4Fe_5S_8$-1000 electrocatalyst.

As shown in Figure S27, the Raman spectrum of P-NSC/$Ni_4Fe_5S_8$-1000 electrocatalyst displayed two main peaks at 1348 and 1574 cm^{-1}, corresponding to the D and G band of carbon, respectively.[2] The relative low intensity ratio of I_D/I_G (0.81) and the obvious 2D peak (2700 cm^{-1}) of carbon signified the carbon network on the P-NSC/$Ni_4Fe_5S_8$-1000 electrocatalyst possessed high graphitization.[3]

References

[1] F. Song, X. Hu, *J. Am. Chem. Soc.*, **2014**, 136, 16481–16484.

[2] Q. Wang, Y. Ji, Y. Lei, Y. Wang, Y. Wang, Y. Li, S. Wang, *ACS Energy Lett.*, **2018**, 3, 1183–1191.

[3] A. C. Ferrari, J. C. Meyer, V. Scardaci, C. Casiraghi, M. Lazzeri, Mauri, F.; S. Piscanec, D. Jiang, K. S. Novoselov, S. Roth, A. K. Geim, *Phys. Rev. Lett.* **2006**, 97, 187401.